Received: 13 July 2021 | Revised: 30 May 2022 | Accepted: 29 June 2022

DOI: 10.1002/elps.202100218

ELECTROPHORESIS

RESEARCH ARTICLE

A $Ti_3C_2T_X$/Pt–Pd based amperometric biosensor for sensitive cancer biomarker detection

Bin Ran[1] | **Chaozhan Chen**[1] | **Bo Liu**[1] | **Minbo Lan**[2] | **Huaying Chen**[3,4] | **Yonggang Zhu**[3,4]

[1]School of Science, Harbin Institute of Technology, Shenzhen, Shenzhen, P. R. China

[2]Shanghai Key Laboratory of Functional Materials Chemistry, School of Chemistry and Molecular Engineering, East China University of Science and Technology, Shanghai, P. R. China

[3]School of Mechanical Engineering and Automation, Harbin Institute of Technology, Shenzhen, Shenzhen, P. R. China

[4]Center for Microflows and Nanoflows, Harbin Institute of Technology, Shenzhen, Shenzhen, P. R. China

Correspondence
Yonggang Zhu, Center for Microflows and Nanoflows, Harbin Institute of Technology, Shenzhen, Shenzhen, 518055, P. R. China.
Email: zhuyonggang@hit.edu.cn

Color online: See the article online to view Figures 1–8 in color.

Funding information
Guangdong Basic and Applied Basic Research Foundation, Grant/Award Number: 2019B1515120037; Shenzhen Science and Technology Innovation Commission, Grant/Award Numbers: JCYJ20170413105329648, JCYJ20200109112801728

Abstract

The detection of cancer biomarkers is of great significance for the early screening of cancer. Detecting the content of sarcosine in blood or urine has been considered to provide a basis for the diagnosis of prostate cancer. However, it still lacks simple, high-precision and wide-ranging sarcosine detection methods. In this work, a $Ti_3C_2T_X$/Pt–Pd nanocomposite with high stability and excellent electrochemical performance has been synthesized by a facile one-step alcohol reduction and then used on a glassy carbon electrode (GCE) with sarcosine oxidase (SO_x) to form a sarcosine biosensor (GCE/$Ti_3C_2T_X$/Pt–Pd/SO_x). The prominent electrocatalytic activity and biocompatibility of $Ti_3C_2T_X$/Pt–Pd enable the SO_x to be highly active and sensitive to sarcosine. Under the optimized conditions, the prepared biosensor has a wide linear detection range to sarcosine from 1 to 1000 μM with a low limit of detection of 0.16 μM (S/N = 3) and a sensitivity of 84.1 μA/mM cm^2. Besides, the reliable response in serum samples shows its potential in the early diagnosis of prostate cancer. More importantly, the successful construction and application of the amperometric biosensor based on $Ti_3C_2T_X$/Pt–Pd will provide a meaningful reference for detecting other cancer biomarkers.

KEYWORDS
electrochemical biosensor, prostate cancer diagnosis, Pt–Pd bimetallic nanoparticles, sarcosine detection, $Ti_3C_2T_X$ MXene

1 | INTRODUCTION

Cancer is one of the greatest health challenges facing human beings. It is killing millions of lives every year, and the number is still increasing rapidly [1]. Early diagnosis can significantly improve cancer patients' treatment effect and survival probability. However, it is hard to

Abbreviations: AA, ascorbic acid; CV, cyclic voltammetry; EDS, energy dispersive spectrometer; EG, ethylene glycol; EIS, electrochemical impedance spectroscopy; GCE, glassy carbon electrode; NPs, nanoparticles; PSA, prostate-specific antigen; Rct, charge transfer resistance; RT, room temperature; SO_x, sarcosine oxidase; UA, uric acid.

identify cancer at an early stage by the conventional methods, including ultrasound, magnetic resonance imaging, and biopsy, as these methods depend on the phenotypic properties of the tumor [2]. Biomarker detection is an effective tool for early cancer diagnosis with the advantages of noninvasiveness and the ability to assess the risk of cancer development [3]. Much effort has been made to study biomarker detection for cancers, some of which are successful in clinical applications [2, 4, 5].

Prostate cancer is the second most frequent cancer and the fifth leading cause of cancer death in men [1]. The prostate-specific antigen (PSA) level in serum (above four ng/ml) has been utilized as a prostate cancer biomarker for about 30 years, and the PSA scanning has brought revolutionary changes to the clinical management of the disease [6]. However, the lack of specificity of PSA (especially when patients have a total PSA in the 4–10-ng/ml "gray zone") may cause false-positive and false-negative diagnoses, as well as conflicting clinical screening trial results, leading to overdiagnosis and overtreatment of prostate cancer [7–9]. Therefore, there is an urgent need to use alternative or extra prostate cancer biomarkers in conjunction with PSA to improve the diagnosis accuracy. Those biomarkers should be able to provide extra information on the aggressiveness of the disease. Sarcosine is an important intermediate in glycine metabolism and could provide an extra indication of cancer progress. It has been proven to be a satisfactory candidate in biomarker panels for early prostate cancer detection and aggressivity prediction [10, 11]. Therefore, sarcosine has been chosen in this study as an extra biomarker to develop prostate cancer detection techniques.

Generally, sarcosine exists in trace amounts in normal human blood, whereas its concentration increases during the progress of prostate cancer, typically at the level of μM [10, 12]. Many techniques can be used to detect sarcosine in this concentration level, such as high-throughput liquid chromatography–mass spectrometry [13, 14], fluorescence spectroscopy [15–18], and colorimetric assay [19–21]. However, the operational complexity, costs, and the needs for trained professional operators are the main obstacles to the large-scale deployments of detection technologies [22]. Electrochemical sensing techniques are highly likely to overcome the issue mentioned previously due to the advantages of simpleness, portability, and general disposability [23]. Recently, several studies have reported simple and inexpensive amperometric biosensors for sarcosine detection [12, 23–26]. These sensors were usually developed by integrating the specific enzymatic and electrochemical reactions. The sensing mechanism is as follows. The sarcosine is converted to glycine, formaldehyde, and H_2O_2 in the presence of the enzyme, that is, sarcosine oxidase (SO_x) (Equation 1). The electrochemical oxidation of H_2O_2 at the electrode interface (Equation 2) leads to a current variation, which can be measured to calculate the concentration of sarcosine:

$$\text{sarcosine} + H_2O + O_2 \xrightarrow{SOx} \text{glycine} + H_2O_2 + \text{formaldehyde} \quad (1)$$

$$H_2O_2 \rightarrow O_2 + 2H^+ + 2e^- \quad (2)$$

To improve the sensitivity of sarcosine detection, various nanomaterials, such as graphene [27, 28], carbon nanotube [29, 30], and metal nanoparticles (NPs) [31, 32], have been applied for electrode modification to facilitate electron transfer reaction. Still and all, these sensors cannot yet achieve highly sensitive detection of sarcosine in a wide concentration range.

$Ti_3C_2T_X$ MXene is a newly developed two-dimensional material that has been widely used in electrochemical biosensors due to its unique properties like layered morphology, high electrical conductivities, excellent mechanical stability, high surface area, and good biocompatibility [33–35]. For example, $Ti_3C_2T_X$ can act as conductive support to immobilize enzymes/proteins to achieve the direct electron transfer between the enzyme and the electrode and enable sensitive biomolecules detection [36]. It can also be used to quantify biomolecules by detecting H_2O_2 produced during the enzymatic reaction [37, 38]. Besides, similar to graphene, it is possible to combine noble metal NPs with $Ti_3C_2T_X$ to increase its surface area and catalytic activity, improving the electrochemical sensor performance. Lorencova et al. [39] reported that the modification of $Ti_3C_2T_X$ with Pt NPs could enhance its stability in an anodic potential window and exhibit high catalytic activity for hydrogen peroxide, ascorbic acid (AA), and so on. Furthermore, owing to the bifunctional or synergistic effects, bimetallic NPs have a significant improvement in chemical selectivity and catalytic activity superior to those of monometallic NPs, which is a fascinating material in the study of electrochemical biosensors [40–43]. Bimetallic NPs, especially Pt–Pd NPs, have been applied with graphene/reduced graphene oxide [44, 45], carbon nanotubes [46], and carbon fiber [47] in electrochemical H_2O_2 sensors and showed an outstanding sensitivity. To date, only a limited number of biosensors based on MXene-bimetallic NPs have been developed. Yao et al. [48] prepared self-supported $Ti_3C_2T_X$ paper decorated with bimetallic NPs for sensitive superoxide detection. However, the synthesis of such materials involves a multistep process, and the sensor constructed from it has limited application scenarios. Further, the bimetallic NPs-modified $Ti_3C_2T_X$ nanocomposites have not been used for cancer biomarker detection.

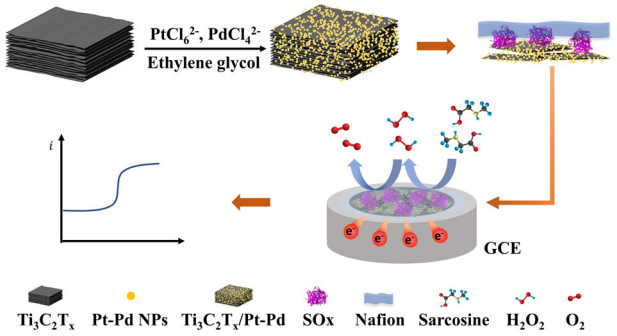

FIGURE 1 Preparation of sarcosine sensing electrode and the sensing mechanism

This study describes a simple method to develop an amperometric sarcosine biosensor for prostate cancer diagnosis based on $Ti_3C_2T_X$/Pt–Pd nanocomposites (Figure 1). In this strategy, the $Ti_3C_2T_X$/Pt–Pd bimetallic nanocomposites were prepared by a facile one-step alcohol reduction process and then applied with SO_x on glassy carbon electrode (GCE) to construct a sarcosine sensing electrode GCE/$Ti_3C_2T_X$/Pt–Pd/SO_x. The SO_x on GCE/$Ti_3C_2T_X$/Pt–Pd/SO_x converted sarcosine to glycine, formaldehyde, and H_2O_2. The current changes caused by the oxidation of H_2O_2 on $Ti_3C_2T_X$/Pt–Pd were used for the quantification of sarcosine. It is the first time to our knowledge that the $Ti_3C_2T_X$/Pt–Pd bimetallic nanocomposites have been used for cancer biomarker detection. Furthermore, owing to the outstanding electrochemical performance and biocompatibility of $Ti_3C_2T_X$/Pt–Pd nanocomposites, the prepared sarcosine biosensor exhibits a wide meaningful detection range with high sensitivity and low limit of detection (LOD) compared to other biosensors reported in the literature.

2 | MATERIALS AND METHODS

2.1 | Materials

Multilayer $Ti_3C_2T_X$ nanosheets were purchased from Nanjing XFNANO Materials Tech Co. Potassium chloroplatinate (K_2PtCl_6), sodium tetrachloropalladate (Na_2PdCl_4), ethylene glycol (EG), and sarcosine were obtained from Aladdin Industrial Corporation. The Nafion 117 solution (5% in a mixture of lower aliphatic alcohols and water) was purchased from Sigma-Aldrich. Potassium ferrocyanide ($K_4Fe(CN)_6$), potassium ferricyanide ($K_3Fe(CN)_6$), hydrogen peroxide (H_2O_2), SO_x, uric acid (UA), glucose (Glu), and AA were purchased from Shanghai Macklin Biochemical Co., Ltd. Normal human serum was obtained from Abbkine Scientific Co., Ltd. All chemicals were analytical grade and used without further purifications. For all of the solution preparations, ultrapure water (18.2 MΩ/cm) was used.

2.2 | Instruments

The scanning electron microscopic (SEM) images and energy-dispersive spectrometer (EDS) mapping images were captured using a ZEISS SUPRA 55 electron microscope (Carl Zeiss, Germany). Transmission electron micrograph (TEM) and selected area electron diffraction (SAED) pattern were taken using a Tecnai G2 spirit electron microscope (FEI, USA). X-ray diffraction (XRD) study was performed using a D8 Advance (Bruker, USA) X-ray diffractometer with Cu K_α radiation ($\lambda = 1.5418$ Å). X-ray photoelectron spectroscopy (XPS) data were collected from PHI 5000 VersaProbe II (PHI, Japan). All electrochemical measurements were carried out in CHI660E electrochemical workstation (Shanghai Chen Hua Instrument Co. Ltd, China).

2.3 | Synthesis of $Ti_3C_2T_X$/Pt–Pd composites

The $Ti_3C_2T_X$/Pt–Pd composite was synthesized by a facile, one-step alcohol reduction process. First, 20-mg $Ti_3C_2T_X$ nanosheets, 24.3-mg K_2PtCl_6 (50 μmol), 14.7-mg Na_2PdCl_4 (50 μmol), and 10-mg trisodium citrate were dispersed in 40-ml EG solutions (50% in water) and deoxygenated by bubbling with pure nitrogen for 30 min. After 20-min ultrasonication, the mixture solution was incubated at 80°C for 6 h with continuous stirring. Then, the black products ($Ti_3C_2T_X$/Pt–Pd) were obtained by centrifugation, washed with water three times, and finally vacuum-dried at room temperature (RT) overnight.

2.4 | Fabrication of the modified electrodes

An amount of 1-mg $Ti_3C_2T_X$ or $Ti_3C_2T_X$/Pt–Pd was dispersed in 100-μl water and sonicated for 10 min to obtain homogeneous dispersions. To avoid oxidation of $Ti_3C_2T_X$, the dispersions were bubbling with nitrogen for 30 min. Before modification, the bare GCE (3-mm diameter) was polished with Al_2O_3 powder (0.3 μm) to a mirror surface, washed with ultrapure water, and dried under nitrogen gas flow. The GCE/$Ti_3C_2T_X$ and GCE/$Ti_3C_2T_X$/Pt–Pd were prepared by covering 10 μl of $Ti_3C_2T_X$ and $Ti_3C_2T_X$/Pt–Pd suspension on the GCE surface, respectively, and dried at RT. The sarcosine sensing electrode GCE/$Ti_3C_2T_X$/Pt–Pd/SO_x was obtained by sequentially drop-casting a certain

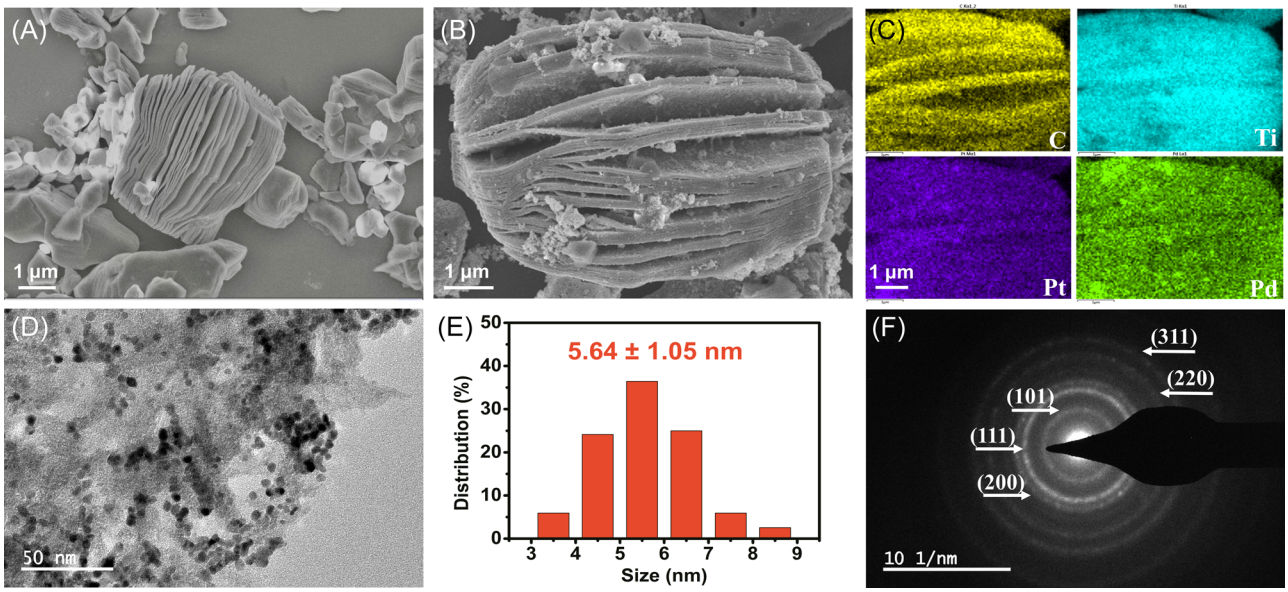

FIGURE 2 Scanning electron microscopic (SEM) images of $Ti_3C_2T_X$ (A), $Ti_3C_2T_X$/Pt–Pd (B), and the energy dispersive spectrometer (EDS) mapping images (C, Ti, Pt, and Pd) of $Ti_3C_2T_X$/Pt–Pd (C). Transmission electron micrograph (TEM) image (D), the Pt–Pd nanoparticles (NPs) size distribution (E), and the selected area electron diffraction (SAED) pattern of $Ti_3C_2T_X$/Pt–Pd (F)

amount of $Ti_3C_2T_X$/Pt–Pd suspension (10 μg/μl), SO_x solution (1 U/μl), and 2.5 μl of 0.05-wt% Nafion solution onto the GCE (3-mm diameter) surface then dried at RT and stored at 4°C before use.

2.5 | Electrochemical measurements

All electrochemical tests were carried out in a three-electrode system as a GCE (3-mm diameter) or the modified electrode as the working electrode, Ag/AgCl (in 3.5-M KCl) electrode as the reference electrode, and a platinum electrode as the counter electrode.

3 | RESULTS AND DISCUSSION

3.1 | Characterization of $Ti_3C_2T_X$/Pt–Pd

The morphologies of $Ti_3C_2T_X$ and $Ti_3C_2T_X$/Pt–Pd were characterized by SEM and TEM (Figure 2). As shown in Figure 2A, the $Ti_3C_2T_X$ is a typical multilayer graphene-like structure, and this unique nanostructure can provide a large surface area for NPs loading. Figure 2B shows that Pt–Pd bimetallic NPs were obviously decorated on $Ti_3C_2T_X$ after the alcohol reduction. EDS mapping images of $Ti_3C_2T_X$/Pt–Pd in Figure 2C confirm the loading of Pt–Pd NPs. Figure 2D shows the TEM image of $Ti_3C_2T_X$/Pt–Pd. It can be seen that the Pt–Pd NPs are uniform and well dispersed on the $Ti_3C_2T_X$ nanosheet, and the average particle size of Pt–Pd NPs is 5.64 ± 1.05 nm (Figure 2E).

The crystalline structure of $Ti_3C_2T_X$/Pt–Pd was characterized by SAED and XRD. An SAED pattern corresponding to Figure 2F clearly shows the reflections of (111), (200), (220), and (311) from Pt–Pd NPs and indicates that it is a polycrystalline structure. The additional reflection peak (101) is attributed to TiO_2, which was produced by the local heat developed at the time of etching of the MAX phase [49]. Figure 3A presents XRD patterns of $Ti_3C_2T_X$ and $Ti_3C_2T_X$/Pt–Pd. The observed diffraction peaks of $Ti_3C_2T_X$ approximate at 2θ values of 8.8°, 18.2°, 27.8°, 35.2°, 41.7°, and 60.7° are associated with (002), (004), (006), (008), (0010), and (110), respectively. The broad peaks reveal that the $Ti_3C_2T_X$ is amorphous to some extent. As for the $Ti_3C_2T_X$/Pt–Pd pattern, three diffraction peaks at 40.1°, 46.6°, and 67.9° are ascribed to (111), (200), and (220) planes of Pt–Pd NPs with the face-centered cubic structure, respectively. However, the addition of Pt–Pd NPs attenuates the diffraction peak of $Ti_3C_2T_X$.

XPS was carried out to investigate the detailed elemental composition and chemical states of the $Ti_3C_2T_X$/Pt–Pd nanocomposites. In the full-survey-scan spectrum in Figure 3B, both $Ti_3C_2T_X$ and $Ti_3C_2T_X$/Pt–Pd consist of the characteristic peaks of C1s, Ti2p, O1s, and F1s. In addition, the presence of two characteristic peaks of Pt4f and Pd3d in $Ti_3C_2T_X$/Pt–Pd confirms the loading of Pt–Pd NPs in the composite. The high-resolution XPS spectra of Pt and Pd elements in $Ti_3C_2T_X$/Pt–Pd were analyzed. Figure 3C shows the deconvolution of the core-level XPS spectrum of Pt4f yielded two pairs of peaks, in which the more intensive peaks at 70.8 and 74.2 eV are attributed to Pt(0), whereas the others at 71.9 and 75.8 eV belong to the Pt(II). For the

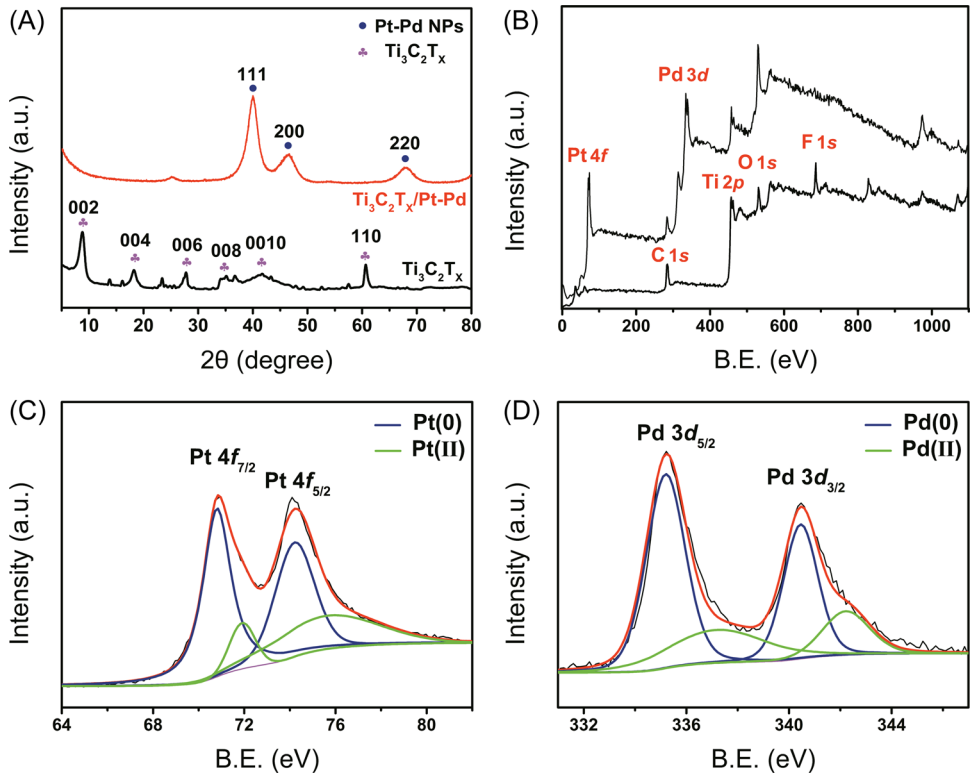

FIGURE 3 X-ray diffraction (XRD) patterns of $Ti_3C_2T_X$ and $Ti_3C_2T_X$/Pt–Pd (A). Full-survey-scan X-ray photoelectron spectroscopy (XPS) spectrum of $Ti_3C_2T_X$/Pt–Pd (B) and the core-level spectrum of Pt4f (C) and Pd3d (D)

Pd3d core-level XPS spectrum in Figure 3D, two doublets at binding energies of 335.2–340.4 and 337.3–342.2 eV are fitted and assigned to the Pd(0) and Pd(II), respectively. According to the peak intensity ratios of Pt(0)–Pt(II) and Pd(0)–Pd(II), metallic Pt(0) and Pd(0) are the predominant species in the $Ti_3C_2T_X$/Pt–Pd. Moreover, the element analysis spectrum shows that the amounts of Pt and Pd in $Ti_3C_2T_X$/Pt–Pd are 1.52 and 1.29, respectively, and their ratio is close to 1:1 (Figure S1).

3.2 | Electrochemical performance of the modified electrode

It was reported that pristine $Ti_3C_2T_X$ could be irreversibly oxidized in the anodic potential window and result in less electrochemical activity [39]. As illustrated in Figure S2, the cyclic voltammetry (CV) experiments show a dramatic decrease in the current of GCE/$Ti_3C_2T_X$ between the 1st and 20th CV scans (89% reduction at +0.6 V). Meanwhile, there is only a 10% current loss of GCE/$Ti_3C_2T_X$/Pt–Pd at +0.6 V after 20 times CV scans. It suggests that the loading of Pt–Pd bimetallic NPs can significantly enhance the stability of $Ti_3C_2T_X$ in an anodic potential window, which enables it to be more widely used in electrochemical sensing.

Figure 4A shows the CV curves of GCE and GCE/$Ti_3C_2T_X$/Pt–Pd at the potential ranges from −0.1 to 0.6 V with a scan rate of 0.05 V/s in 5-mM $K_3Fe(CN)_6$ solution containing 0.1-M KCl. The redox current of GCE/$Ti_3C_2T_X$/Pt–Pd is significantly higher than that of bare GCE. The peak current is proportional to the electroactive surface area of the working electrode and can be expressed by the Randles–Sevcik equation: $I_p = 2.69 \times 10^5 AD^{1/2}n^{3/2}\vartheta^{1/2}C$, where I_p (A) is the peak current; A (cm^2) is the electroactive surface area of the electrode; D is the diffusion coefficient (6.7×10^{-6} cm^2/s for $[Fe(CN)_6]^{3-}$; n is the number of electrons transferred in the redox reaction, which is 1 for $[Fe(CN)_6]^{3-/4-}$; ϑ (V/s) is the scan rate, and C (mol/cm^3) is the concentration of the redox reactant. The calculated electroactive surface areas of bare GCE and GCE/$Ti_3C_2T_X$/Pt–Pd are 0.05518 and 0.08748 cm^2. These results reveal that $Ti_3C_2T_X$/Pt–Pd nanocomposites have good conductivity and large surface area and are expected to be used as the base material for enzyme-based biosensors.

The electrochemical impedance spectroscopy (EIS) of GCE and GCE/$Ti_3C_2T_X$/Pt–Pd was measured in 10 mM of $Fe(CN)_6^{3-/4-}$ solution containing 0.1-M KCl with the frequency ranging from 1 MHz to 0.01 Hz, and the Nyquist plots are displayed in Figure 4B. The charge transfer resistance (R_{ct}) of the electrode is inversely proportional

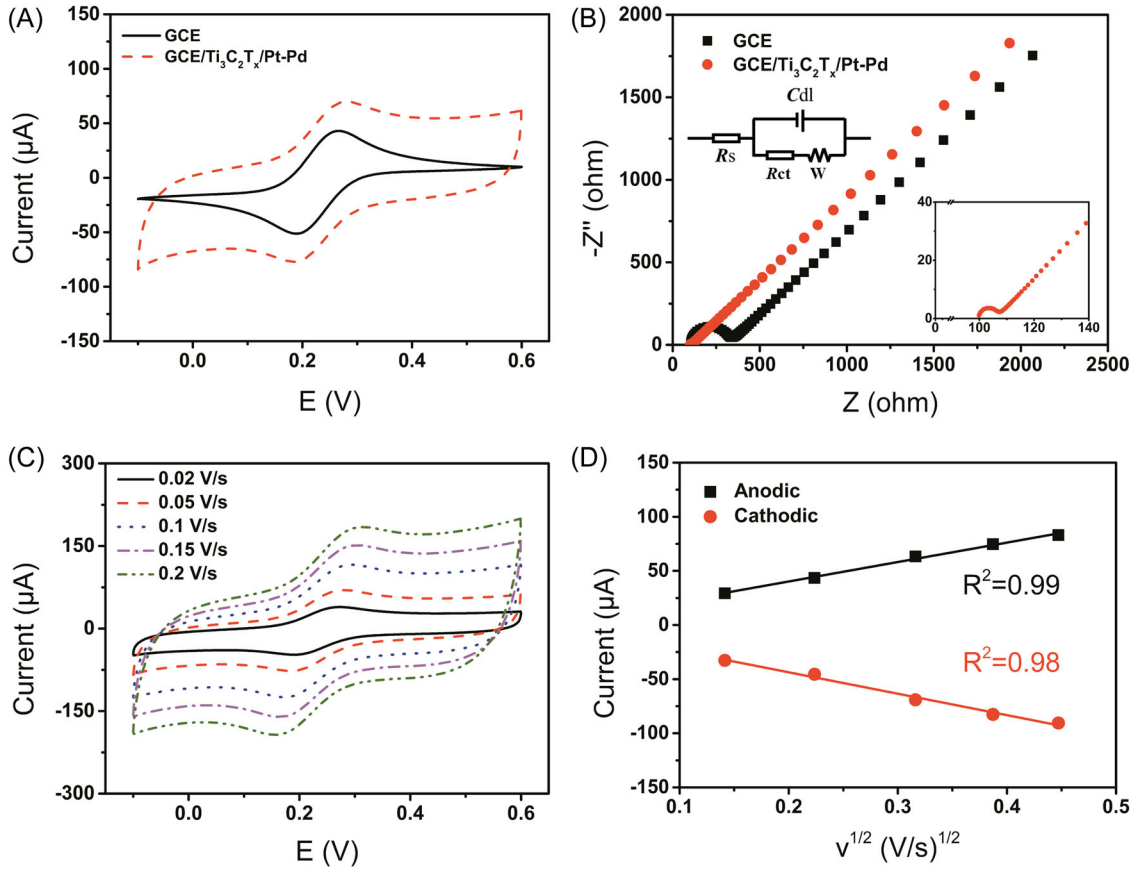

FIGURE 4 (A) Cyclic voltammetry (CV) of glassy carbon electrode (GCE) and GCE/$Ti_3C_2T_X$/Pt–Pd at a scan rate of 50 mV/s in 5-mM $K_3Fe(CN)_6$ solution (containing 0.1-M KCl), and their electrochemical impedance spectroscopy (EIS) (B) in 10-mM $Fe(CN)_6^{3-/4-}$ solution (containing 0.1 M KCl) with the frequency ranging from 1 MHz to 0.01 Hz. (C) CV of GCE/$Ti_3C_2T_X$/Pt–Pd in 5-mM $K_3Fe(CN)_6$ solution (containing 0.1-M KCl) at scan rates from 0.02 to 0.2 V/s, and the relationship between the square root of the scan rate and peak current (D)

to the electron transfer rate, which can be obtained through the equivalent circuit simulation of the EIS curve. Generally, the R_{ct} of the electrode surface is equal to the semicircle diameter of the Nyquist diagram [50]. The result shows that the R_{ct} of the modified electrode GCE/$Ti_3C_2T_X$/Pt–Pd (6.7 Ω) is much lower than that of the bare GCE (230 Ω) and also lower than the reported R_{ct} of GCE/$Ti_3C_2T_X$ (48.58 Ω) [51], reflecting the high surface area and remarkable electron transmission capability of $Ti_3C_2T_X$/Pt–Pd. The CV curves of GCE/$Ti_3C_2T_X$/Pt–Pd in 5-mM $K_3Fe(CN)_6$ solution with the scan rates from 0.02 to 0.2 V/s and the relationship between the scan rate and the anodic/cathodic peaks' current are shown in Figure 4C,D, respectively. Figure 4C shows that the shape of the CV curves is well preserved as the scan rate is varied, which indicates the rapid mass transport at the electrode/electrolyte interface [25, 52]. In addition, the favorable linear relationship between the anodic/cathodic peaks' current and the square root of the scan rate in Figure 4D indicates that the electrochemical reaction on the surface of GCE/$Ti_3C_2T_X$/Pt–Pd is controlled by the diffusion of the electroactive species [52].

3.3 | Detection of H_2O_2

The outstanding electrochemical performance of GCE/$Ti_3C_2T_X$/Pt–Pd makes it a useful nonenzymatic sensor for detecting H_2O_2. Figure S3 shows the CV curve of GCE/$Ti_3C_2T_X$/Pt–Pd in 0.1-M PBS (pH 7.4) with and without H_2O_2. When a CV scan was performed in PBS without H_2O_2, the result showed a typical CV curve of Pt-based material and a broad peak at about +0.1 V owing to the reduction of Pt–Pd NPs. After 5-mM H_2O_2 was added, the oxidation and reduction current of GCE/$Ti_3C_2T_X$/Pt–Pd increased significantly. Additionally, the oxidation of H_2O_2 on GCE/$Ti_3C_2T_X$/Pt–Pd started at +0.32 V, whereas a much higher overpotential is needed on the conventional solid electrode (~0.8 V vs. Ag/AgCl) [53], indicating an outstanding electrocatalytic activity of $Ti_3C_2T_X$/Pt–Pd toward H_2O_2. The amperometric curve of GCE/$Ti_3C_2T_X$/Pt–Pd for successive additions of H_2O_2 into 0.1-M PBS (pH 7.4) at +0.4 V was recorded. As shown in Figure 5A, the sensor can quickly respond to the added H_2O_2 and reach a steady current in a short time. Figure 5B shows that the response current is

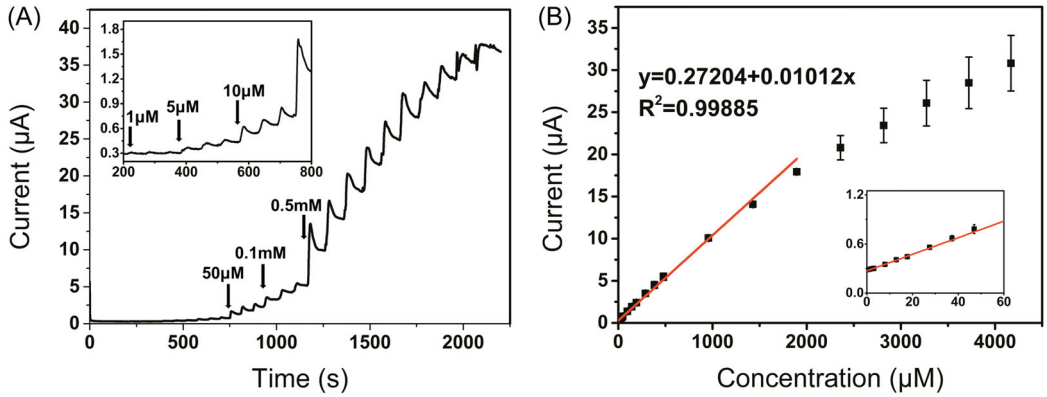

FIGURE 5 The amperometric curve of glassy carbon electrode (GCE)/$Ti_3C_2T_X$/Pt–Pd in 0.1-M PBS (pH 7.4) successive addition of H_2O_2 at +0.4 V (A). The corresponding linear relationship between the H_2O_2 concentration and response current (B) and the partially enlarged view (inset of B)

proportional to the concentration of H_2O_2 in the range of 1–1896 μM. The linear regression equation and sensitivity are I (μA) = 0.01012C (μM) + 0.27204 (R^2 = 0.998), and 144.6 μA/mM cm^2, respectively. Furthermore, the GCE/$Ti_3C_2T_X$/Pt–Pd has a lower LOD (0.35 μM, S/N = 3) than the reported GCE/$Ti_3C_2T_X$/Pt (0.448 μM) [39]. These results reveal the high performance of GCE/$Ti_3C_2T_X$/Pt–Pd in the electrochemical detection of H_2O_2, which enables it to be further applied in an enzyme-based biosensing platform.

3.4 | Optimization of biosensor performance

The amperometric sarcosine biosensor was constructed based on GCE/$Ti_3C_2T_X$/Pt–Pd/SO_x. Prior to the amperometric analysis of sarcosine, the experimental parameters that may affect the analytical performance of the biosensor during the preparation process are optimized. The optimal amount of $Ti_3C_2T_X$/Pt–Pd and SO_x on the GCE/$Ti_3C_2T_X$/Pt–Pd/SO_x was studied by comparing the response current in 100-μM sarcosine solution (0.1-M PBS, pH 7.4) at +0.4 V. Figure 6A displays the biosensor fabricated with 10 μl of $Ti_3C_2T_X$/Pt–Pd suspension (10 μg/μl) has the highest response current. It can be attributed to the sufficient amount of catalytic material on the surface of GCE to form a uniform and efficient sensing layer, whereas a larger amount of material will agglomerate and cannot function effectively and even attenuate the response signal. As depicted in Figure 6B, when the amount of SO_x in the biosensor increases to 5 μl (1 U/μl), the response current reaches the maximum. However, an excessive SO_x causes a decrease in current as the SO_x can act as resistance material. Therefore, 10 μl of $Ti_3C_2T_X$/Pt–Pd suspension (10 μg/μl) and 5 μl of SO_x solution (1 U/μl) were used in the preparation of the sarcosine biosensor. The morphology of the sensing electrode prepared with the previous parameters was characterized by SEM. Figure S4A,B shows the SEM images of GCE/$Ti_3C_2T_X$/Pt–Pd and GCE/$Ti_3C_2T_X$/Pt–Pd/SO_x, respectively. It can be seen that, compared with the GCE/$Ti_3C_2T_X$/Pt–Pd, most of $Ti_3C_2T_X$/Pt–Pd on the GCE/$Ti_3C_2T_X$/Pt–Pd/SO_x is covered by SO_x to form a uniform coating.

The influence of pH on the sarcosine biosensor was tested in 50-μM sarcosine solution (0.1-M PBS) at various pH values. As shown in Figure 6C, the response current gradually increases from pH 5.0 to 8.0, and the highest magnitude of the current response is obtained at pH 8.0, which is the same as the reported optimal pH for the SO_x catalytic reaction [54]. Considering the difference in response current between pH 7 and pH 8 is negligible, and the pH value of blood samples is usually around 7.4, pH 7.4 was selected as the suitable working pH in the following experiments.

3.5 | Amperometric detection of sarcosine

The amperometric curve of the prepared sarcosine biosensor was recorded in 0.1-M PBS (pH 7.4) with a successive addition of sarcosine at the applied potential of +0.4 V (see Figure 7A). It shows that the response current gradually increases with the addition of sarcosine solution, indicating that sarcosine is catalyzed by SO_x to produce H_2O_2, and then H_2O_2 was oxidized with the electrocatalysis of $Ti_3C_2T_X$/Pt–Pd. As Figure 7B shows, a quality linear relationship exists between the response current and the sarcosine concentrations in a wide range from 1 to 1000 μM. The linear regression equation is I (μA) = 0.00589C (μM) + 0.21086 (R^2 = 0.997). The sensitivity, LOD, and LOQ of the biosensor are 84.1 μA/mM cm^2, 0.16 μM (S/N = 3), and 0.53 μM (S/N = 10), respectively. Table 1 shows the

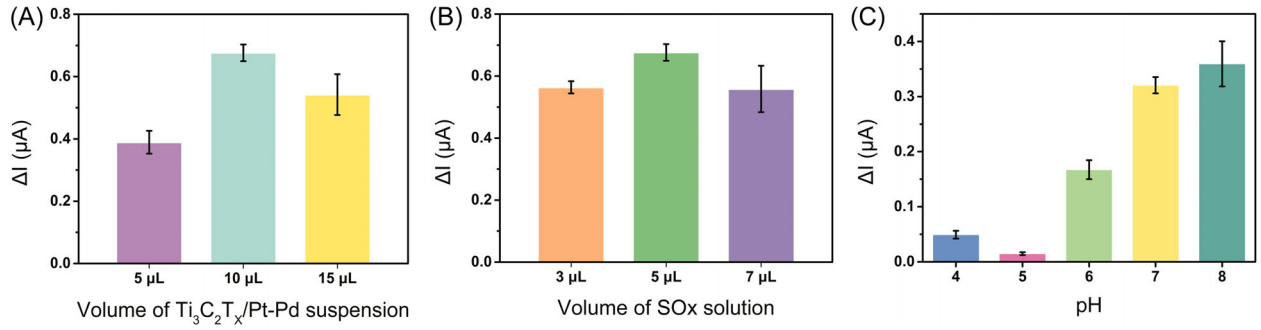

FIGURE 6 The response currents of glassy carbon electrode (GCE)/$Ti_3C_2T_X$/Pt–Pd/sarcosine oxidase (SO_x) prepared with different volumes of $Ti_3C_2T_X$/Pt–Pd suspension (10 μg/μl, 5-μl SO_x solution was used) (A) and SO_x (1 U/μl, 10 μl $Ti_3C_2T_X$/Pt–Pd suspension was used) (B) in 100-μM sarcosine solution (0.1-M PBS, pH 7.4). (C) The response currents of GCE/$Ti_3C_2T_X$/Pt–Pd/SO_x in 50-μM sarcosine solution (0.1-M PBS) with different pHs

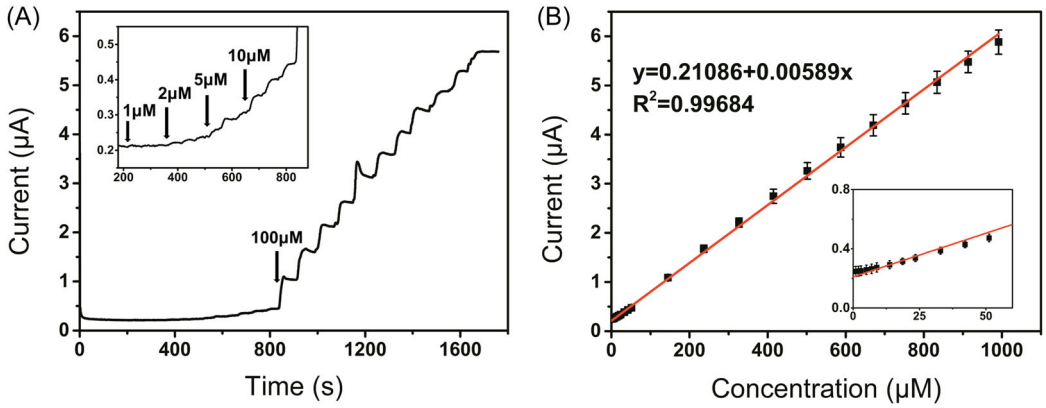

FIGURE 7 The amperometric curve of the prepared biosensor in 0.1-M PBS (pH 7.4) with successive addition of sarcosine (A). The corresponding linear relationship between the sarcosine concentration and response current (B) and the partially enlarged view (inset of B). All the tests were performed at +0.4 V.

TABLE 1 Comparison between different electrochemical sarcosine sensors

Sensor	Sensor type	Linear range (μM)	LOD (μM)	Sensitivity (μA/mM cm²)	Ref.
1	SCPE/Au NPs/MIP	0.011–17.9	0.008	N/A	[55]
2	AuE/SO_x NPs	0.1–100	0.01	N/A	[56]
3	GCE/Pt-Fe3O4@C/SO_x	0.5–60	0.43	48.8	[57]
4	GCE/MNP/Pt/SO_x	5–40	0.24	123.51	[32]
5	AuE/CNTs/Pd-Pt/SO_x	5–60	1.28	17.1	[30]
6	Pt/CNT/SO_x	6–750	6	16.6	[29]
7	GCE/$Ti_3C_2T_X$/Pt–Pd/SO_x	1–1000	0.16	84.1	**This work**

Abbreviations: GCE, glassy carbon electrode; LOD, limit of detection; NPs, nanoparticles.

comparison of the performance of the developed sarcosine biosensor with several other sensors. It can be seen that although Sensor 1 to Sensor 3 has lower or comparable LOD, their linear range is much narrower than that of the currently developed sensor [55–57]. Sensor 4 has a higher sensitivity than the current sensor; however, the linear range is much smaller [32]. Sensors 5 and 6 are inferior to our sensor due to the poorer performance in LOD, linear range, and sensitivity [29, 30].

3.6 | Selectivity, reproducibility, and stability of the sarcosine biosensor

The selectivity of the sensing platform is crucial to real sample analysis. Thus, the selectivity of the sarcosine biosensor to several common interfering analytes was tested. Figure S5 shows the current responses upon successive addition of 50-μM sarcosine, NaCl, KCl, AA, UA, glucose, and a mixture containing all of them into 0.1-M

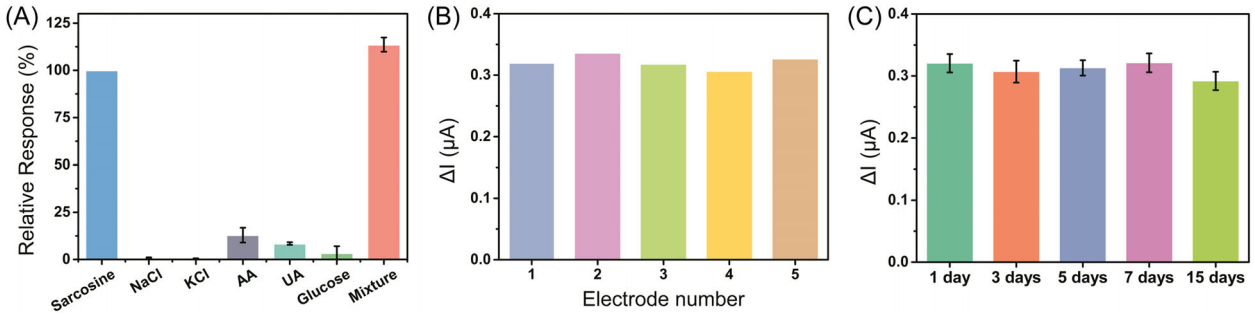

FIGURE 8 The columnar interference error analysis of sarcosine detection (A). The response currents in 50-μM sarcosine at five glassy carbon electrode (GCE)/$Ti_3C_2T_X$/Pt–Pd/sarcosine oxidase (SO_x) electrodes that prepared in the same condition (B). The response currents to 50-μM sarcosine at GCE/$Ti_3C_2T_X$/Pt–Pd/SO_x after storage at different times (C).

PBS (pH 7.4). The columnar error analysis in Figure 8A turns out that the response of these species to the sarcosine amperometric detection is negligible, owing to the combination of the selective enzyme and the anti-interference Nafion layer on the biosensor and the low applied potential (+0.4 V).

The reproducibility of the sarcosine biosensor was evaluated by amperometry in 50-μM sarcosine solution at five sensing electrodes of GCE/$Ti_3C_2T_X$/Pt–Pd/SO_x, as shown in Figure 8B. The relative standard deviation (RSD) of sarcosine detection is 3.4%, which means the good reproducibility of this sensing platform for sarcosine detection.

Additionally, the long-term stability of GCE/$Ti_3C_2T_X$/Pt–Pd/SO_x is crucial for maintaining the sensing properties of the biosensor. Figure 8C shows the response current of the biosensor to 50-μM sarcosine after being stored at 4°C for different times (1d, 3d, 5d, 7d, and 15d). The results indicate that the biosensor can maintain 91% of the initial response after 15 days, illustrating the satisfying stability. It can be attributed to the enhanced electrochemical stability of the $Ti_3C_2T_X$ decorated with Pt–Pd NPs and its excellent biocompatibility to maintain the enzymatic activity of SO_x.

3.7 | Detection of sarcosine in spiked human serum samples

The developed biosensor was tested to detect sarcosine in human serum (diluted 20 times with 0.1-M PBS solution) by a standard addition method. Three spiked samples were obtained by adding sarcosine solution, with final sarcosine concentrations of 19.96, 108.80, and 300.68 μM, respectively. Table 2 shows the recovery and RSD of the sarcosine detection. It can be seen that the recovery rate for these three spiked samples is 98.07%, 98.02%, and 94.06%, respectively, and the corresponding RSD is 1.08%, 1.81%, and 3.79%, respectively. The results show that the biosensor is reliable for detecting sarcosine in serum samples, indicating that it has the potential for early prostate cancer screening.

TABLE 2 The recovery and relative standard deviation (RSD) of sarcosine in serum samples

No.	Added (μM)	Found (μM)	Recovery (%)	RSD (%)
1	19.96	19.61	98.07	1.08
2	108.80	98.03	98.02	1.81
3	300.68	282.18	94.06	3.79

4 | CONCLUDING REMARKS

This study developed an amperometric sarcosine biosensor based on $Ti_3C_2T_X$/Pt–Pd nanocomposites prepared by simple procedures. The Pt–Pd bimetallic NPs were loaded on $Ti_3C_2T_X$ nanosheet by a facile one-step alcohol reduction. The resulting $Ti_3C_2T_X$/Pt–Pd nanocomposites can be easily applied to the surface of GCE to construct an electrochemical sensing interface and exhibit high stability and electrochemical performance. The sensing electrode is formed by coating SO_x on the surface of GCE/$Ti_3C_2T_X$/Pt–Pd. The biosensor has been tested and demonstrated a wide linear range from 1 to 1000 μM, low LOD of 0.16 μM, and high sensitivity of 84.1 μA/mM cm^2. The overall performance of the biosensor is superior to those reported, especially in terms of clinical applications. The current biosensor exhibits excellent selectivity to sarcosine in the presence of a variety of interfering substances and has a good recovery rate for sarcosine detection in serum samples. The good performance of the developed biosensor makes it a potential technique in the early screening of prostate cancer.

ACKNOWLEDGMENT

This work was supported by the Guangdong Basic and Applied Basic Research Foundation (Grant

no. 2019B1515120037) and Shenzhen Science and Technology Innovation Commission (Grant nos. JCYJ20170413105329648 and JCYJ20200109112801728).

CONFLICT OF INTEREST

The authors have declared no conflict of interest.

DATA AVAILABILITY STATEMENT

The data that support the findings of this study are available from the corresponding author upon reasonable request.

ORCID

Yonggang Zhu https://orcid.org/0000-0002-5419-9508

REFERENCES

1. Bray F, Ferlay J, Soerjomataram I, Siegel RL, Torre LA, Jemal A. Global cancer statistics 2018: GLOBOCAN estimates of incidence and mortality worldwide for 36 cancers in 185 countries. CA Cancer J Clin. 2018;68:394–424.
2. Jayanthi V, Das AB, Saxena U. Recent advances in biosensor development for the detection of cancer biomarkers. Biosens Bioelectron. 2017;91:15–23.
3. Ma Y, Gamagedara S. Biomarker analysis for oncology. Biomark Med. 2015;9:845–50.
4. Yin Z, Zhu L, Lv Z, Li M, Tang D. Persistent luminescence nanorods-based autofluorescence-free biosensor for prostate-specific antigen detection. Talanta. 2021;233:122563.
5. Zhu L, Lv Z, Yin Z, Li M, Tang D. Digital multimeter-based point-of-care immunoassay of prostate- specific antigen coupling with a flexible photosensitive pressure sensor. Sens Actuators B. 2021;343:130121.
6. Saini S. PSA and beyond: alternative prostate cancer biomarkers. Cell Oncol. 2016;39:97–106.
7. Prensner JR, Rubin MA, Wei JT, Chinnaiyan AM. Beyond PSA: the next generation of prostate cancer biomarkers. Sci Transl Med. 2012;4:127.
8. Koo KM, Mainwaring PN, Tomlins SA, Trau M. Merging new-age biomarkers and nanodiagnostics for precision prostate cancer management. Nat Rev Urol. 2019;16:302–17.
9. Srivastava S, Koay EJ, Borowsky AD, De Marzo AM, Ghosh S, Wagner PD, et al. Cancer overdiagnosis: a biological challenge and clinical dilemma. Nat Rev Cancer. 2019;19:349–58.
10. Sreekumar A, Poisson LM, Rajendiran TM, Khan AP, Cao Q, Yu J, et al. Metabolomic profiles delineate potential role for sarcosine in prostate cancer progression. Nature. 2009;457:910–4.
11. Jentzmik F, Stephan C, Miller K, Schrader M, Erbersdobler A, Kristiansen G, et al. Sarcosine in urine after digital rectal examination fails as a marker in prostate cancer detection and identification of aggressive tumours. Eur Urol. 2010;58:12–8.
12. Roy A, Chen YP, Qiu JT, Maikap S. Sarcosine prostate cancer biomarker detection by controlling oxygen in NiO_x membrane on vertical silicon nanowires in electrolyte-insulator-nanowire structure. Anal Chem. 2020;92:8064–71.
13. Meyer TE, Fox SD, Issaq HJ, Xu X, Chu LW, Veenstra TD, et al. A reproducible and high-throughput HPLC/MS method to separate sarcosine from alpha- and beta-alanine and to quantify sarcosine in human serum and urine. Anal Chem. 2011;83:5735–40.
14. Chen SE, Hu J, Yan P, Sun J, Jia W, Zhu S, et al. 12-plex UHPLC-MS/MS analysis of sarcosine in human urine using integrated principle of multiplex tags chemical isotope labeling and selective imprint enriching. Talanta. 2021;224:121788.
15. Heger Z, Cernei N, Krizkova S, Masarik M, Kopel P, Hodek P, et al. Paramagnetic nanoparticles as a platform for FRET-based sarcosine picomolar detection. Sci Rep. 2015;5:8868.
16. Luo Y, Wang J, Yang L, Gao T, Pei R. *In vitro* selection of DNA aptamers for the development of fluorescent aptasensor for sarcosine detection. Sens Actuators B. 2018;276:128–35.
17. Sun NN, Yan B. A fluorescent probe based on a Tb(3+)/Cu(2+) co-functionalized MOF for urinary sarcosine detection. Analyst. 2018;143:2349–55.
18. Li W, Li T, Chen S, Deng D, Ji Y, Li R. Nanozyme-mediated cascade reaction system for ratiometric fluorescence detection of sarcosine. Sens Actuators B. 2022;355:131341.
19. Lan J, Xu W, Wan Q, Zhang X, Lin J, Chen J, et al. Colorimetric determination of sarcosine in urine samples of prostatic carcinoma by mimic enzyme palladium nanoparticles. Anal Chim Acta. 2014;825:63–68.
20. Xue Z, Yin B, Wang H, Li M, Rao H, Liu X, et al. An organic indicator functionalized graphene oxide nanocomposite-based colorimetric assay for the detection of sarcosine. Nanoscale. 2016;8:5488–96.
21. Mbage B, Li Y, Si H, Zhang X, Li Y, Wang X, et al. Fabrication of folate functionalized polyoxometalate nanoparticle to simultaneously detect H_2O_2 and sarcosine in colorimetry. Sens Actuators B. 2020;304:127429.
22. Sun J, He Y, He S, Liu D, Lu K, Yao W, et al. A self-powered photoelectrochemical cathodic molecular imprinting sensor based on Au@TiO_2 nanorods photoanode and Cu_2O photocathode for sensitive detection of sarcosine. Biosens Bioelectron. 2022;204:114056.
23. Ding Z, Wang D, Chen L, Zhou H, Zhang X, Feng X, et al. Oxygen-insensitive peroxide reduction catalysts for reliable electrochemical bioassays. Adv Mater Interfaces. 2022;9:2102163.
24. Rebelo TS, Pereira CM, Sales MG, Noronha JP, Costa-Rodrigues J, Silva F, et al. Sarcosine prostate cancer biomarker detection by controlling oxygen in NiOx membrane on vertical silicon nanowires in electrolyte-insulator-nanowire structure. Anal Chim Acta. 2014;850:26–32.
25. Wang Q, Zhao Y, Yang Q, Du D, Yang H, Lin Y. Amperometric sarcosine biosensor with strong anti-interference capabilities based on mesoporous organic-inorganic hybrid materials. Biosens Bioelectron. 2019;141:111431.
26. Song P, Shen J, Ye D, Dong B, Wang F, Pei H, et al. Programming bulk enzyme heterojunctions for biosensor development with tetrahedral DNA framework. Nat Commun. 2020;11:838.
27. Xue Z, Wang H, Rao H, He N, Wang X, Liu X, et al. Amperometric indicator displacement assay for biomarker monitoring: indirectly sensing strategy for electrochemically inactive sarcosine. Talanta. 2017;167:666–71.
28. Liu T, Fu B, Chen J, Li K. An electrochemical sarcosine sensor based on biomimetic recognition. Mikrochim Acta. 2019;186:136.
29. Pannell MJ, Doll EE, Labban N, Wayu MB, Pollock JA, Leopold MC. Versatile sarcosine and creatinine biosensing schemes uti-

lizing layer-by-layer construction of carbon nanotube-chitosan composite films. J Electroanal Chem. 2018;814:20–30.
30. Chen C, Ran B, Wang Z, Zhao H, Lan M, Chen H, et al. Development of micropillar array electrodes for highly sensitive detection of biomarkers. RSC Adv. 2020;10:41110–9.
31. Uhlirova D, Stankova M, Docekalova M, Hosnedlova B, Kepinska M, Ruttkay-Nedecky B, et al. A rapid method for the detection of sarcosine using SPIONs/Au/CS/SOX/NPs for prostate cancer sensing. Int J Mol Sci. 2018;19:3722.
32. Wang Q, Yang C, Yang Q, Yu S, Yang H. Platinum-loaded mesoporous nickel phosphonate and its electrochemical application for sarcosine detection. Anal Chim Acta. 2019;1046:93–8.
33. Sinha A, Dhanjai ZH, Huang Y, Lu X, Chen J, Jain R. MXene: an emerging material for sensing and biosensing. TrAC Trends Anal Chem. 2018;105:424–35.
34. Kalambate PK, Gadhari NS, Li X, Rao Z, Navale ST, Shen Y, et al. Recent advances in MXene–based electrochemical sensors and biosensors. TrAC Trends Anal Chem. 2019;120:115643.
35. Chen J, Tong P, Huang L, Yu Z, Tang D. Ti_3C_2 MXene nanosheet-based capacitance immunoassay with tyramine-enzyme repeats to detect prostate-specific antigen on interdigitated micro-comb electrode. Electrochim Acta. 2019;319:375–81.
36. Liu J, Jiang X, Zhang R, Zhang Y, Wu L, Lu W, et al. MXene-enabled electrochemical microfluidic biosensor: applications toward multicomponent continuous monitoring in whole blood. Adv Funct Mater. 2018;29:1807326.
37. Rakhi RB, Nayak P, Xia C, Alshareef HN. Novel amperometric glucose biosensor based on MXene nanocomposite. Sci Rep. 2016;6:36422.
38. Hroncekova S, Bertok T, Hires M, Jane E, Lorencova L, Vikartovska A, et al. Ultrasensitive Ti_3C_2TX MXene/chitosan nanocomposite-based amperometric biosensor for detection of potential prostate cancer marker in urine samples. Processes. 2020;8:580.
39. Lorencova L, Bertok T, Filip J, Jerigova M, Velic D, Kasak P, et al. Highly stable Ti_3C_2Tx (MXene)/Pt nanoparticles-modified glassy carbon electrode for H_2O_2 and small molecules sensing applications. Sens Actuators B. 2018;263:360–8.
40. Janyasupab M, Liu CW, Zhang Y, Wang KW, Liu CC. Bimetallic Pt-M (M = Cu, Ni, Pd, and Rh) nanoporous for H_2O_2 based amperometric biosensors. Sens Actuators B. 2013;179:209–14.
41. Zhu X, Niu X, Zhao H, Tang J, Lan M. Immobilization of superoxide dismutase on Pt-Pd/MWCNTs hybrid modified electrode surface for superoxide anion detection. Biosens Bioelectron. 2015;67:79–85.
42. Wang Z, Zhao H, Chen K, Li H, Lan M. Sandwich-type electrochemical aptasensor based on hollow mesoporous carbon spheres loaded with porous dendritic Pd@Pt nanoparticles as signal amplifier for ultrasensitive detection of cardiac troponin I. Anal Chim Acta. 2021;1188:339202.
43. Dhara K, Mahapatra DR. Recent advances in electrochemical nonenzymatic hydrogen peroxide sensors based on nanomaterials: a review. J Mater Sci. 2019;54:12319–57.
44. Hossain MF, Park JY. Amperometric glucose biosensor based on Pt-Pd nanoparticles supported by reduced graphene oxide and integrated with glucose oxidase. Electroanalysis. 2014;26:940–51.
45. Zhang F, Liu Z, Han Y, Fan L, Guo Y. Sandwich electrochemical carcinoembryonic antigen aptasensor based on signal amplification of polydopamine functionalized graphene conjugate Pd-Pt nanodendrites. Bioelectrochemistry. 2021;142:107947.
46. Chen KJ, Chandrasekara Pillai K, Rick J, Pan CJ, Wang SH, Liu CC, et al. Bimetallic PtM (M = Pd, Ir) nanoparticle decorated multi-walled carbon nanotube enzyme-free, mediatorless amperometric sensor for H (2)O(2). Biosens Bioelectron. 2012;33:120–7.
47. Li H, Zhao H, He H, Shi L, Cai X, Lan M. Pt-Pd bimetallic nanocoral modified carbon fiber microelectrode as a sensitive hydrogen peroxide sensor for cellular detection. Sens Actuators B. 2018;260:174–82.
48. Yao Y, Lan L, Liu X, Ying Y, Ping J. Spontaneous growth and regulation of noble metal nanoparticles on flexible biomimetic MXene paper for bioelectronics. Biosens Bioelectron. 2020;148:111799.
49. Rakhi RB, Ahmed B, Anjum D, Alshareef HN. Direct chemical synthesis of MnO_2 nanowhiskers on transition-metal carbide surfaces for supercapacitor applications. ACS Appl Mater Interfaces. 2016;8:18806–14.
50. Suni II. Impedance methods for electrochemical sensors using nanomaterials. TrAC Trends Anal Chem. 2008;27:604–11.
51. Xia T, Liu G, Wang J, Hou S, Hou S. MXene-based enzymatic sensor for highly sensitive and selective detection of cholesterol. Biosens Bioelectron. 2021;183:113243.
52. Huang B, Wang H, Liang S, Qin H, Li Y, Luo Z, et al. Two-dimensional porous cobalt–nickel tungstate thin sheets for high performance supercapattery. Energy Storage Mater. 2020;32:105–14.
53. Wang X, Zhang X. Electrochemical co-reduction synthesis of graphene/nano-gold composites and its application to electrochemical glucose biosensor. Electrochim Acta. 2013;112:774–82.
54. Zhao G, Jorns MS. Spectral and kinetic characterization of the michaelis charge transfer complex in monomeric sarcosine oxidase. Biochemistry. 2006;45:5985–92.
55. Nguy TP, Van Phi T, Tram DTN, Eersels K, Wagner P, Lien TTN. Development of an impedimetric sensor for the label-free detection of the amino acid sarcosine with molecularly imprinted polymer receptors. Sens Actuators B. 2017;246:461–70.
56. Kumar P, Narwal V, Jaiwal R, Pundir CS. Construction and application of amperometric sarcosine biosensor based on SOxNPs/AuE for determination of prostate cancer. Biosens Bioelectron. 2018;122:140–6.
57. Yang Q, Li N, Li Q, Chen S, Wang HL, Yang H. Amperometric sarcosine biosensor based on hollow magnetic Pt-Fe3O4@C nanospheres. Anal Chim Acta. 2019;1078:161–7.

SUPPORTING INFORMATION

Additional supporting information can be found online in the Supporting Information section at the end of this article.

How to cite this article: Ran B, Chen C, Liu B, Lan M, Chen H, Zhu Y. A $Ti_3C_2T_X$/Pt–Pd based amperometric biosensor for sensitive cancer biomarker detection. Electrophoresis. 2022;43:2033–2043.
https://doi.org/10.1002/elps.202100218